FIRST RESULTS FROM THE LICK AGN MONITORING PROJECT: THE MASS OF THE BLACK HOLE IN ARP 151

Misty C. Bentz,[1] Jonelle L. Walsh,[1] Aaron J. Barth,[1] Nairn Baliber,[2,3] Nicola Bennert,[2,4] Gabriela Canalizo,[4,5]
Alexei V. Filippenko,[6] Mohan Ganeshalingam,[6] Elinor L. Gates,[7] Jenny E. Greene,[8,9] Marton G. Hidas,[2,3]
Kyle D. Hiner,[4,5] Nicholas Lee,[6] Weidong Li,[6] Matthew A. Malkan,[10] Takeo Minezaki,[11] Frank J. D. Serduke,[6]
Joshua H. Shiode,[6] Jeffrey M. Silverman,[6] Thea N. Steele,[6] Daniel Stern,[12] Rachel A. Street,[2,3]
Carol E. Thornton,[1] Tommaso Treu,[2,13] Xiaofeng Wang,[6,14] Jong-Hak Woo,[2,9,10] and Yuzuru Yoshii[11,15]

ABSTRACT

We have recently completed a 64 night spectroscopic monitoring campaign at the Lick Observatory 3 m Shane telescope with the aim of measuring the masses of the black holes in 13 nearby ($z < 0.05$) Seyfert 1 galaxies with expected masses in the range $\sim 10^6$–$10^7 \, M_\odot$. We present here the first results from this project—the mass of the central black hole in Arp 151. Strong variability throughout the campaign led to an exceptionally clean Hβ lag measurement in this object of $4.25^{+0.68}_{-0.66}$ days in the observed frame. Coupled with the width of the Hβ emission line in the variable spectrum, we determine a black hole mass of $(7.1 \pm 1.2) \times 10^6 \, M_\odot$, assuming the Onken et al. normalization for reverberation-based virial masses. We also find velocity-resolved lag information within the Hβ emission line which clearly shows infalling gas in the Hβ-emitting region. Further detailed analysis may lead to a full model of the geometry and kinematics of broad line region gas around the central black hole in Arp 151.

Subject headings: galaxies: active — galaxies: individual (Arp 151) — galaxies: nuclei — galaxies: Seyfert

1. INTRODUCTION

Reverberation mapping (Blandford & McKee 1982; Peterson 1993) is the most successful method employed for measuring the central black hole mass in type 1 active galactic nuclei (AGNs). Rather than relying on spatially resolved observations, reverberation mapping resolves the influence of the black hole in the time domain through spectroscopic monitoring of changes in the continuum flux and the delayed response, or "echo," in the broad emission lines. The time lag between these changes, τ, depends on the light-travel time across the broad-line region (BLR). Combining the radius of the BLR, $c\tau$, with the velocity width of the broad emission line gives the virial mass of the central black hole.

To date, successful reverberation-mapping studies have been carried out for approximately 36 active galaxies (compiled by Peterson et al. 2004, 2005), mostly probing black hole masses

in the range 10^7–$10^9 \, M_\odot$. Studies of lower mass AGNs have been restricted by their lower luminosities, requiring telescopes larger than the typical 1.5 m apertures that have been employed. With the goal of extending the mass range probed by reverberation studies, we have carried out a 64 night spectroscopic monitoring campaign on the Lick Observatory 3 m Shane telescope, targeting 13 AGNs with expected black hole masses in the range $\sim 10^6$–$10^7 \, M_\odot$. We present here the first results from this project: an analysis of the Hβ reverberation in the nearby ($z = 0.0211$) Seyfert galaxy Arp 151 (Mrk 40). Full campaign details and results will be presented in a series of forthcoming papers.

2. OBSERVATIONS

2.1. *Photometry*

Broadband Johnson *B* images of Arp 151 were obtained at the 32 inch Tenagra II telescope in southern Arizona most nights between calendar dates 2008 February 26 and May 15. Typical exposure times were 2×300 s.

The images were reduced following standard techniques. The flux of the AGN was measured through a circular aperture of radius 4.35″, and differential photometry was obtained relative to 8 stars within the field.[16] Absolute flux calibrations were determined on a photometric night using the Landolt SA 101 and SA 109 standard star fields. The calibrated light curve is shown in Figure 1. For the cross-correlation analysis, the *B*-band magnitudes were converted to fluxes.

2.2. *Spectroscopy*

Spectroscopic monitoring was carried out at the Lick Observatory 3 m Shane telescope with the Kast dual spectrograph. Arp 151 was observed from March 24–May 20 on a total of 43 nights. We restricted our observations to the Kast red-side

[1] Department of Physics and Astronomy, 4129 Frederick Reines Hall, University of California, Irvine, CA 92697; mbentz@uci.edu.

[2] Physics Department, University of California, Santa Barbara, CA 93106.

[3] Las Cumbres Observatory Global Telescope, 6740 Cortona Drive, Suite 102, Goleta, CA 93117.

[4] Institute of Geophysics and Planetary Physics, University of California, Riverside, CA 92521.

[5] Department of Physics and Astronomy, University of California, Riverside, CA 92521.

[6] Department of Astronomy, University of California, Berkeley, CA 94720-3411.

[7] Lick Observatory, P.O. Box 85, Mount Hamilton, CA 95140.

[8] Princeton University Observatory, Princeton, NJ 08544.

[9] Hubble Fellow.

[10] Department of Physics and Astronomy, University of California, Los Angeles, CA 90024.

[11] Institute of Astronomy, School of Science, University of Tokyo, 2-21-1 Osawa, Mitaka, Tokyo 181-0015, Japan.

[12] Jet Propulsion Laboratory, California Institute of Technology, MS 169-527, 4800 Oak Grove Drive, Pasadena, CA 91109.

[13] Sloan Fellow, Packard Fellow.

[14] Physics Department and Tsinghua Center for Astrophysics (THCA), Tsinghua University, Beijing 100084, China.

[15] Research Center for the Early universe, School of Science, University of Tokyo, 7-3-1 Hongo, Bunkyo-ku, Tokyo 113-0033, Japan.

[16] A simple model of the host-galaxy surface brightness profile from the ground-based images indicates that ~40% of the light within this aperture comes from the host-galaxy starlight.
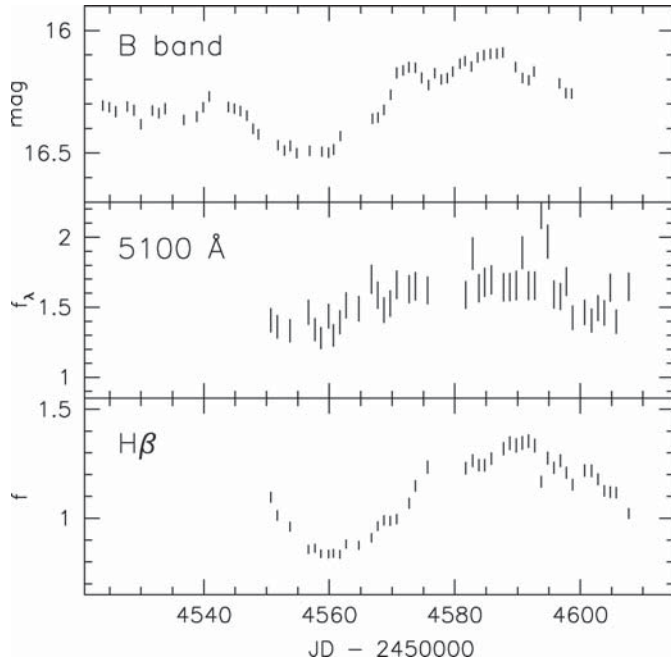
FIG. 1.—Light curves for Arp 151. From top to bottom, the panels are: B-band magnitude, observed continuum flux density at rest-frame 5100 Å, and Hβ emission-line flux. The units are as given in Table 1 for 5100 Å and Hβ.

CCD and employed the 600 line mm^{-1} grating with spectral coverage over the range 4300–7100 Å. Spectra were obtained at a fixed position angle of 90° through a 4″ wide slit. Exposures were usually 2 × 600 s at an air mass of ~1.1, resulting in a typical signal-to-noise ratio (S/N) of ~100 per pixel at rest-frame 5100 Å in the combined spectra. The images were reduced with IRAF and the spectra were extracted with a width of 13 pixels (10.1″), with sky regions of width 6 pixels beginning at a distance of 19 pixels. Flux calibrations were determined from nightly spectra of standard stars.

To mitigate the effects of slit losses and variable seeing and transparency, we employed the spectral scaling algorithm of van Groningen & Wanders (1992) to scale the total flux of the narrow [O III] λλ4959, 5007 doublet in each individual spectrum to match the [O III] flux in a reference spectrum created from the spectra obtained on the 10 nights with the best weather and seeing conditions. This method accounts for differences in the overall flux scale, as well as small wavelength shifts and small differences in spectral resolution, and has been shown to result in spectrophotometric accuracies of ~2% (Peterson et al. 1998a).

Finally, the spectroscopic light curves were measured. The continuum flux was measured in the observed-frame window 5187–5227 Å (rest-frame 5100 Å). The flux in this window is a combination of the AGN continuum flux, which is variable, and a constant component from the host-galaxy starlight. The Hβ flux was measured by fitting a linear continuum under the Hβ emission line, determined from the continuum flux at 4850–4900 Å and 5175–5225 Å, and then integrating the emission-line flux above the continuum from 4900–5050 Å. This technique includes the flux contribution from the narrow Hβ emission line, which is simply a constant offset. The resultant light curves are presented in Figure 1, with statistical properties listed in Table 1. Figure 2 shows the mean and root-mean-square (rms) spectra, where the rms spectrum shows the standard deviation of all the spectra relative to the mean spectrum (i.e., the variable components of the spectra).

TABLE 1
LIGHT-CURVE STATISTICS

Time Series (1)	N (2)	T_{median} (3)	$\langle f \rangle$[a] (4)	$\langle \sigma_f / f \rangle$ (5)
B band	60	1.03	1.46 ± 0.04	0.0197
5100 Å	43	1.02	1.58 ± 0.18	0.0614
Hβ	43	1.02	1.14 ± 0.19	0.0241

NOTES.—Col. (1): Feature. Col. (2): Number of observations. Col. (3): Median sampling rate in days. Col. (4): Mean flux and standard deviation. Col. (5): Mean fractional error.

[a] Flux densities are in units of 10^{-15} ergs s^{-1} cm^{-2} Å^{-1}; emission-line fluxes are in units of 10^{-13} ergs s^{-1} cm^{-2}.

3. ANALYSIS

3.1. *Time-Series Analysis*

For the time-series analysis, we place more emphasis on the B-band light curve as the driving, continuum light curve, although we also consider the lower S/N light curve of the 5100 Å flux. To determine the average time lag between variations in the continuum flux and variations in the Hβ emission-line flux, we follow the standard practice of cross-correlating the light curves using the interpolation cross-correlation function (ICCF) method (Gaskell & Sparke 1986; Gaskell & Peterson 1987) as well as the discrete correlation function (DCF) method (Edelson & Krolik 1988), with the White & Peterson (1994) modifications to both. The resulting cross-correlation functions are shown in Figure 3. The uncertainties in the time lag are determined using the Monte Carlo "flux randomization/random subset sampling" method described by Peterson et al. (1998b, 2004). In short, the method samples a random subset of the data points in the light curves, randomizes the fluxes by applying a Gaussian deviation within the flux uncertainties, and cross-correlates the modified light curves. The procedure is carried out 1000 times, and a distribution of lag measurements is built up. We include two specific measurements of the lag in Table 2: τ_{peak}, the location of the maximum of the cross-correlation function r_{max}; and τ_{cent}, the centroid of the points near the peak of the function with $r \geq 0.8 r_{max}$. The uncertainties on τ_{peak} and τ_{cent} are set such that 15.87% of the Monte Carlo realizations fall below the range indicated by the uncertainties, and 15.87% fall above this range (i.e., 1 σ uncertainties for a Gaussian distribution). We measure an average observed-frame lag of $\tau_{cent} = 4.25^{0.68}_{0.66}$ days between the B-band and Hβ light curves. The values listed in Table 2 are corrected for time dilation effects.
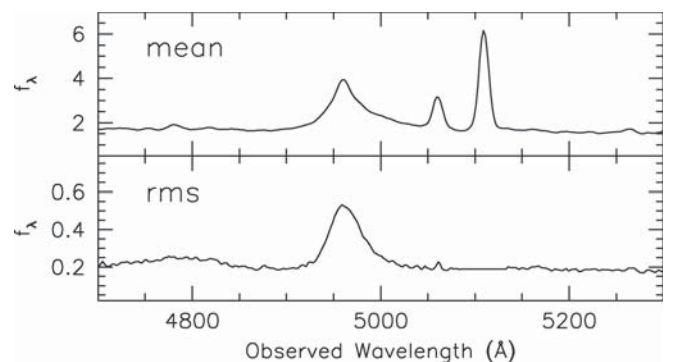

FIG. 2.—Mean and variable (rms) spectra of Arp 151 in the Hβ region. The narrow lines have been removed from the rms spectrum.
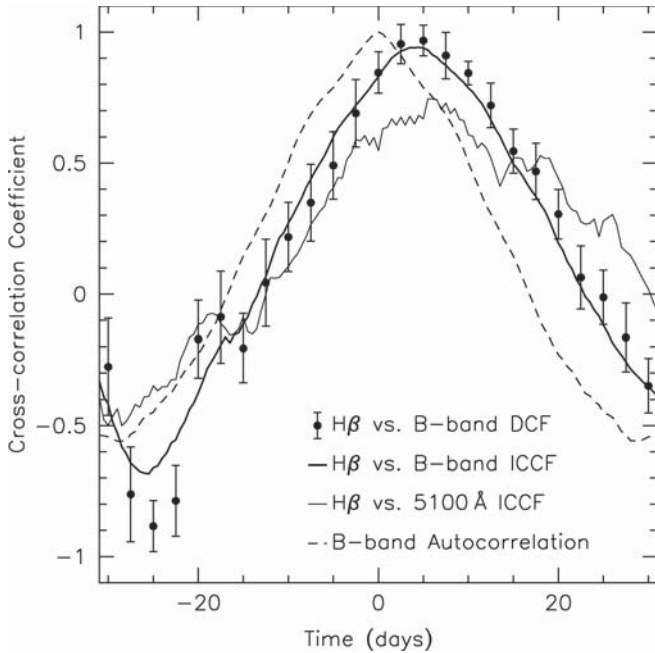
FIG. 3.—Cross-correlation functions for Arp 151. The heavy line is the cross-correlation of the B-band flux and Hβ emission, and the data points show the discrete correlation between the same. The cross-correlation of the 5100 Å flux and Hβ (thin solid line), while noisier, is consistent. The dashed line is the B-band auto-correlation function, which peaks at zero lag as expected.

3.2. *Line Width Measurement*

The width of the broad Hβ emission line was measured in the mean and rms spectra. We report here two separate measures of the line width: the full-width at half-maximum flux (FWHM) and the line dispersion, $\sigma_{\rm line}$, which is the second moment of the emission-line profile (Peterson et al. 2004). The uncertainties in the line widths are again set using Monte Carlo random subset sampling methods. In this case, a random subset of the spectra is chosen and a mean and rms spectrum are created, from which the FWHM and $\sigma_{\rm line}$ are measured. A distribution of line-width measurements is built up through 1000 realizations, from which we take the mean and the standard deviation to be the line width and its typical uncertainty, respectively. Additional systematic errors, such as those due to the exact determination of the continuum contribution, are not included in these estimates of the uncertainty. The line widths presented in Table 2 have been corrected for the resolution of the spectrograph following Peterson et al. (2004).

3.3. *Black Hole Mass*

Following the usual assumption that the BLR kinematics are gravitationally driven, the black hole mass is determined via the virial equation

$$M_{\rm BH} = f \frac{c\tau v^2}{G}, \tag{1}$$

where τ is the mean time delay for the region of interest (here, the Hβ-emitting region), v is the velocity of gas in that region, c is the speed of light, G is the gravitational constant, and f is a scaling factor of order unity that depends on the detailed geometry and kinematics of the region.

With the premise that the $M_{\rm BH}$-$\sigma_\star$ relationship for local, quiescent galaxies holds for AGNs and their host galaxies, Onken

TABLE 2
REST-FRAME REVERBERATION MEASUREMENTS

Measurement	Value
$\tau_{\rm cent}$	4.17 $_{0.64}^{0.67}$ days
$\tau_{\rm peak}$	3.67 $_{0.24}^{0.74}$ days
$\sigma_{\rm line}$ (mean)	1738 ± 10 km s^{-1}
FWHM (mean)	2842 ± 59 km s^{-1}
$\sigma_{\rm line}$ (rms)	1261 ± 37 km s^{-1}
FWHM (rms)	2283 ± 143 km s^{-1}
$c\tau v^2/G$	1.3 ± 0.2 10^6 $M_\odot$
$M_{\rm BH}$	7.1 ± 1.2 10^6 $M_\odot$

et al. (2004) find that $\langle f \rangle \approx 5.5$ for reverberation-based masses. This particular scaling is appropriate when $\tau_{\rm cent}$ and $\sigma_{\rm line,rms}$ are used for the lag and line width in the black hole mass determination. For the measurements presented here, the Onken et al. normalization gives $M_{\rm BH} = (7.1 \pm 1.2) \times 10^6$ $M_\odot$. Individual reverberation masses, however, are subject to a typical factor of 2–3 uncertainty (Onken et al.), likely due to differences in the intrinsic, but unknown, f-value for each individual system. Also listed in Table 2 is the "virial product," assuming $f = 1$. The black hole mass in Arp 151 is smaller than the estimate based on the stellar velocity dispersion ($\sigma_\star = 124 \pm 12$ km s^{-1}; Greene & Ho 2006) and the $M_{\rm BH}$-$\sigma_\star$ relationship of Tremaine et al. (2002) which predicts $2.0_{1.0}^{1.7} \times 10^7$ $M_\odot$, but the two are consistent within the known scatter for reverberation-based masses and the $M_{\rm BH}$-$\sigma_\star$ relationship.

4. VELOCITY-RESOLVED TIME DELAY MEASUREMENTS

A key goal of reverberation mapping is to recover the full transfer function (time delay vs. velocity structure) responsible for the shape of the emission-line light curve in response to the driving continuum light curve. Determining the transfer function is the most promising method to potentially provide detailed information on the geometry and kinematics of the BLR. While some hints of the transfer function shape have been seen in certain high-quality reverberation data sets (i.e., Horne et al. 1991), a full recovery of the transfer function has not yet been achieved.

We carried out an initial analysis of the velocity-resolved time lag information for Arp 151 by binning the Hβ emission line in velocity space, where each of the eight bins contained an equal amount of variable flux. Eight light curves were created, one for each velocity bin, and the light curves were each cross-correlated with the B-band light curve using the methods in § 3.1. Figure 4 shows the results of this analysis: there is a clear gradient in the gas response where the blueshifted Hβ emission lags the response in the redshifted Hβ emission. This is the typical signature of radial infall: the gas on the far side of the AGN is moving toward us, and the gas on the near side is moving away from us. Outflowing (i.e., wind-driven) gas would produce the opposite effect (short lags blueshifted and long lags redshifted) while pure rotation would produce a symmetric pattern around zero velocity. Only outflow specifically precludes a determination of $M_{\rm BH}$ due to the nongravitational motion of the BLR gas. While the kinematics of the BLR Hβ-emitting gas in Arp 151 show a strong signature of radial infall, a full two-dimensional echo map of the velocity and time delay structure in the spectra (e.g., Welsh & Horne 1991) must be recovered before we can fully explain the details of the BLR geometry and kinematics. Such an effort is beyond the scope of this Letter, but is currently being pursued.

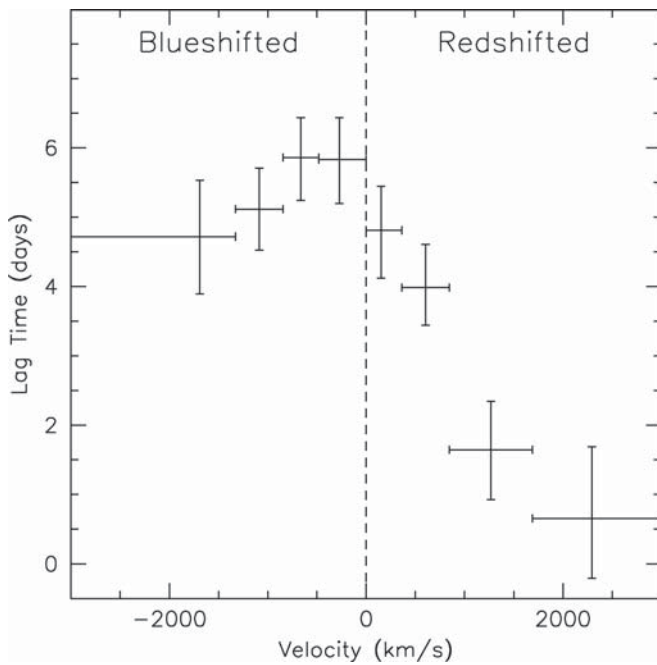The results presented here demonstrate the clearest signature

Fig. 4.—Velocity-resolved Hβ lag measurements for Arp 151. The error bars in the lag direction are the 1 σ uncertainties on the lag measurements, while in the velocity direction they show the size of the velocity bin (which extend to the line integration limits on both sides). A clear signature of blue-shifted gas with long lags and redshifted gas with short lags is detected, indicating radial infall of BLR gas.

value of $\langle f \rangle \approx 5.5$ is determined empirically and is independent of specific BLR models. Subsumed into the population average, $\langle f \rangle$, are the signatures of kinematic and geometric states that are common among AGNs with reverberation results. While it is almost certain that the individual details of each BLR will result in somewhat different intrinsic f-values for every AGN (e.g., Collin et al. 2006), there is currently no reason to expect that the f-value for Arp 151 is wildly discrepant from the population average, or to suspect the mass derived here of having uncertainties larger than those typically expected for reverberation masses.

5. SUMMARY

We have presented the first light curves and reverberation analysis from our AGN monitoring campaign at Lick Observatory. We detect a clear lag in the broad Hβ emission-line response to changes in the continuum flux for Arp 151, and we present a measurement of the black hole mass assuming the Onken et al. (2004) normalization. Initial analysis of velocity-resolved time delays in the Hβ line shows a strong signature of infalling gas, but further work is needed to map out the detailed structure and kinematics of the BLR in Arp 151.

We see strong variability in other emission lines, including Hα, Hγ, and He II, the analysis of which will be included in future papers. In addition, we have a *Hubble Space Telescope* Cycle 17 program to image the host galaxies of the AGNs in this sample, allowing us to correct their spectroscopic luminosities for starlight and apply these new results to the low end of the radius-luminosity relationship for AGNs (Bentz et al. 2006, 2008), which is the primary calibration for all single-epoch mass estimates for broad-lined AGNs.

of gravitational infall in the BLR of an AGN to date. Some indications of infalling gas have been seen in the C IV broad line response in other objects, such as NGC 5548 (e.g., Crenshaw & Blackwell 1990; Done & Krolik 1996) and Fairall 9 (Koratkar & Gaskell 1989). As such, AGN BLRs seem to commonly exhibit signatures of infalling gas (but see Maoz et al. 1991; Kollatschny 2003). The f-value in equation (1) is directly dependent on the kinematics of the BLR, thereby resulting in a different f-value for an AGN BLR with radial infall than for a BLR with Keplerian rotation. The Onken et al. (2004)

REFERENCES

Bentz, M. C., et al. 2006, ApJ, 644, 133
———. 2008, ApJ, submitted
Blandford, R. D., & McKee, C. F. 1982, ApJ, 255, 419
Collin, S., et al. 2006, A&A, 456, 75
Crenshaw, D. M., & Blackwell, J. H., Jr. 1990, ApJ, 358, L37
Done, C., & Krolik, J. H. 1996, ApJ, 463, 144
Edelson, R. A., & Krolik, J. H. 1988, ApJ, 333, 646
Gaskell, C. M., & Peterson, B. M. 1987, ApJS, 65, 1
Gaskell, C. M., & Sparke, L. S. 1986, ApJ, 305, 175
Greene, J. E., & Ho, L. C. 2006, ApJ, 641, L21
Horne, K., Welsh, W. F., & Peterson, B. M. 1991, ApJ, 367, L5
Kollatschny, W. 2003, A&A, 407, 461

Koratkar, A. P., & Gaskell, C. M. 1989, ApJ, 345, 637
Maoz, D., et al. 1991, ApJ, 367, 493
Onken, C. A., et al. 2004, ApJ, 615, 645
Peterson, B. M. 1993, PASP, 105, 247
Peterson, B. M., et al. 1998a, ApJ, 501, 82
———. 1998b, PASP, 110, 660
———. 2004, ApJ, 613, 682
———. 2005, ApJ, 632, 799
Tremaine, S., et al. 2002, ApJ, 574, 740
van Groningen, E., & Wanders, I. 1992, PASP, 104, 700
Welsh, W. F., & Horne, K. 1991, ApJ, 379, 586
White, R. J., & Peterson, B. M. 1994, PASP, 106, 879